Optimizing Interface Conductivity in Electronics

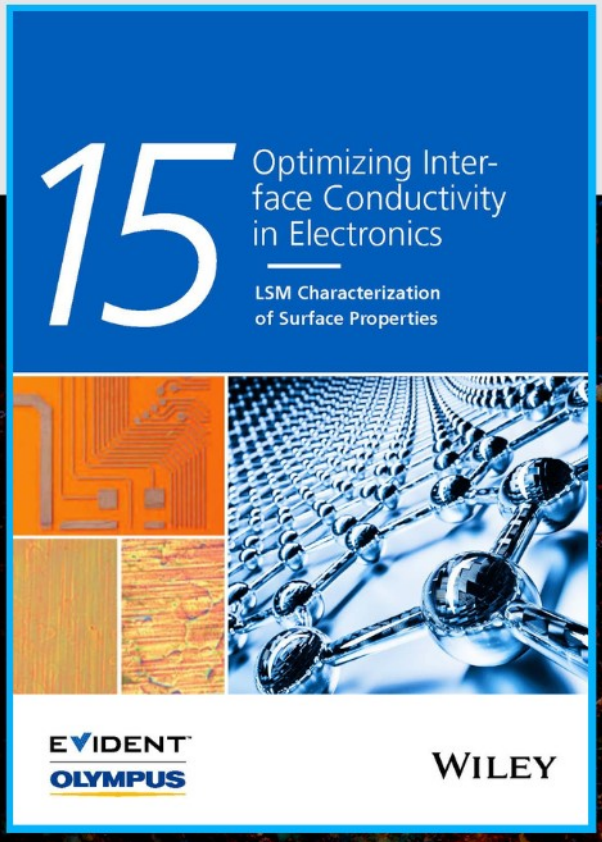

The latest eBook from Advanced Optical Metrology. Download for free.

Surface roughness is a key parameter for judging the performance of a given material's surface quality for its electronic application. A powerful tool to measure surface roughness is 3D laser scanning confocal microscopy (LSM), which will allow you to assess roughness and compare production and finishing methods, and improve these methods based on mathematical models.

Focus on creating high-conductivity electronic devices with minimal power loss using laser scanning microscopy is an effective tool to discern a variety of roughness parameters.

EVIDENT
OLYMPUS

WILEY

ADVANCED FUNCTIONAL MATERIALS
www.afm-journal.de

Alternating Magnetic Field-Enhanced Triboelectric Nanogenerator for Low-Speed Flow Energy Harvesting

Baosen Zhang, Qi Gao, Wenbo Li, Mingkang Zhu, Hengyu Li, Tinghai Cheng,* and Zhong Lin Wang**

Low-speed flow energy, such as breezes and rivers, which are abundant in smart agriculture and smart cities, faces significant challenges in efficient harvesting as an untapped sustainable energy source. This study proposes an alternating magnetic field-enhanced triboelectric nanogenerator (AMF-TENG) for low-speed flow energy harvesting, and demonstrates its feasibility through experimental results. AMF-TENG's minimum cut-in speed is 1 m s^{-1}, thereby greatly expanding its wind energy harvesting range. When the wind speed is 1–5 m s^{-1}, the open-circuit voltage (V_{OC}) is 20.9–179.3 V. The peak power is 0.68 mW at 5 m s^{-1}. In a durability test of 100 K cycles, the V_{OC} decreases from 188.4 to 174.2 V but remain at 92.5% of the initial value. furthermore, the AMF-TENG can harvest low-speed flow energy from the natural environment to power temperature and humidity sensors and wireless light intensity sensor in smart agriculture. This study provides a promising method for low-speed flow energy harvesting in distributed applications.

1. Introduction

The issues of environmental pollution and the energy crisis have spurred a growing desire for sustainable energy sources among humans.[1] Wind and hydroelectric power have been extensively researched and applied as sustainable energy sources due to their large reserves and lack of pollution.[2] Previously, wind power and hydropower relied on electromagnetic power generation technology, which required high flow rates for electricity production. Traditional wind energy harvesting devices were optimized for high wind speeds (>5 m s^{-1}), which are only prevalent in a few areas or at high altitudes.[3] Consequently, low-speed wind energy in many regions and at low altitudes remains underutilized.[4] Nevertheless, widespread low-speed wind energy or water flow energy is expected to resolve the issue of power supply for Internet of Things (IoT) sensors, and it is a distributed sustainable energy that needs to be developed urgently.[5] Therefore, innovative energy harvesting methods are needed to effectively harness this low-speed flow energy and overcome the associated challenges.

Triboelectric nanogenerator (TENG) based on triboelectrification effect and electrostatic induction coupling was invented by Wang's group in 2012.[6] Low cost and simplicity make TENGs ideal for harvesting low-frequency weak mechanical energy.[7] Several studies have demonstrated the ability of TENGs to harvest wind and water flow energy.[8] TENGs for fluid energy harvesting can be broadly classified into two categories, namely rotational and flow-induced vibration.[9] Studies have shown that TENGs based on the principle of flow-induced vibration tend to exhibit lower cut-in velocities at low flow speeds, but the open structure is not suitable for long-term work in outdoor environments.[10] The rotational TENGs can continue to work in a long-term outdoor harsh environment due to their sealed shell protection and the separation of the energy harvesting unit from the power generation unit. However, the electrostatic adsorption force between the materials of the TENGs results in a large cut-in speed.[11] Therefore, reducing the cut-in velocity of rotational TENGs is an important challenge for TENG to effectively harvest energy at low flow speed, which has great meaning for promoting the practical use of TENG in powering distributed Internet of Things.

Here, a strategy based on an alternating magnetic field for harvesting energy from low-speed flow is proposed. The coil generates an induced current in an alternating magnetic field due to the principle of electromagnetic induction. According to the magnetic effect of the current, the magnetic field generated by the energized coil interacts with the alternating magnetic field to generate periodic attractive and repulsive forces, thereby driving the TENG-based generation unit. Since the low-velocity fluid does not directly act on the power generation unit, the energy-harvesting structure can be started at a low flow speed. Thus, the

B. Zhang, Q. Gao, W. Li, M. Zhu, H. Li, T. Cheng, Z. L. Wang
Beijing Institute of Nanoenergy and Nanosystems
Chinese Academy of Sciences
Beijing 101400, China
E-mail: lihengyu@binn.cas.cn; chengtinghai@binn.cas.cn; zhong.wang@mse.gatech.edu
B. Zhang, Q. Gao, W. Li, T. Cheng
School of Nanoscience and Engineering
University of Chinese Academy of Sciences
Beijing 100049, China
H. Li
College of Materials Science and Opto-Electronics Technology
University of Chinese Academy of Sciences
Beijing 100049, China
Z. L. Wang
Georgia Institute of Technology
Atlanta, GA 30332-0245, USA

The ORCID identification number(s) for the author(s) of this article can be found under https://doi.org/10.1002/adfm.202304839

DOI: 10.1002/adfm.202304839

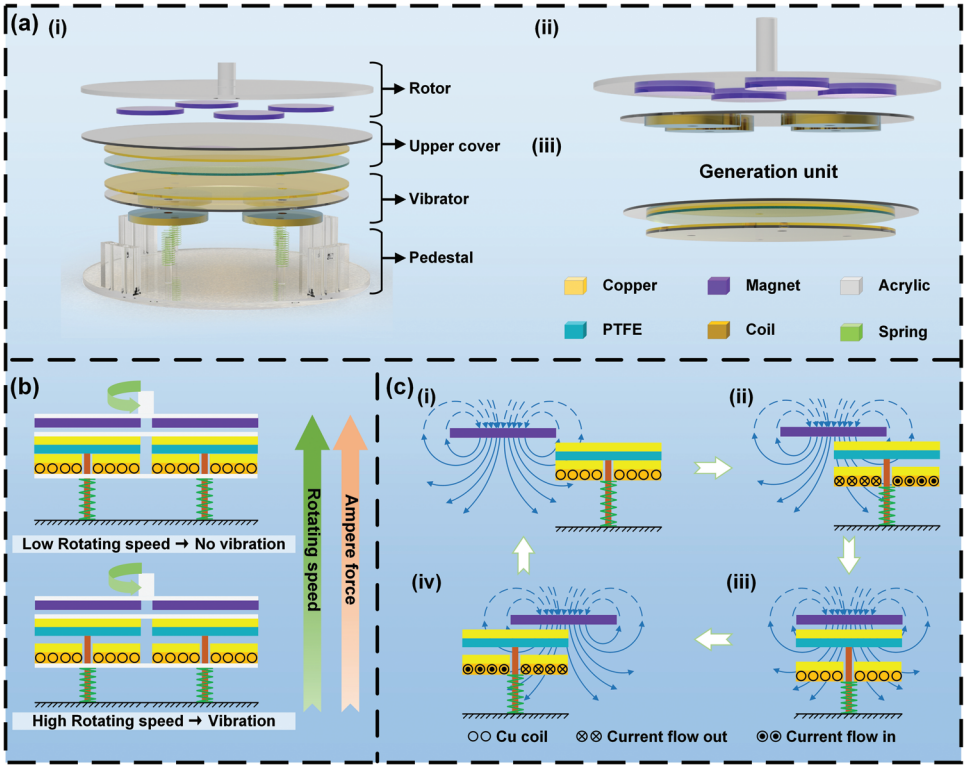

Figure 1. The structure of alternating magnetic field-enhanced triboelectric nanogenerator (AMF-TENG) and the principle of ampere-force driven generation unit. a) Structure display of AMF-TENG for low-speed flow energy harvesting. b) The principle of alternating magnetic fields to drive the vibration of the generation unit. c) Four typical working states of the vibrator under the action of ampere force on the coils.

cut-in speed of the rotational TENG is effectively reduced. Based on this strategy, an alternating magnetic field-enhanced TENG (AMF-TENG) is developed to collect fluid energy at low flow speeds. The experiments demonstrate the feasibility of using the ampere force to drive TENG work. We use wind energy, which has lower energy density than water flow, as the energy source, and achieved a cut-in wind speed of 1 m s^{-1}, greatly extending the effective collection range of rotational TENG in low-velocity machinery. The open-circuit voltage (V_{OC}) is 20.9 to 179.3 V at wind speeds of 1–5 m s^{-1}. The peak power is 0.68 mW at 5 m s^{-1}. The V_{OC} of AMF-TENG remains at about 92.5% after continuous operation for 100 K cycles. Low-speed wind energy harvesting is realized to power temperature and humidity sensor and wireless light intensity sensor. As a result of this method, TENGs have a new strategy for harvesting low-speed wind energy and water flow energy, which will promote the development and utilization for distributed sustainable energy.

2. Results and Discussion

2.1. Structural Design and Operation Principle

Distributed energy sources play a vital role in self-powered sensing systems. Although low-speed flow energy is commonly dispersed in the environment, it is difficult to harvest it efficiently. **Figure 1**a(i) explodes to show the structure of AMF-TENG. The uppermost part is a rotor equipped with magnets, which can be connected to various energy capture devices, such as wind scoops or water wheels, through the top shaft [Figure 1a(ii)]. The upper cover and the vibrator constitute a generation unit (contact-separated TENG) [Figure 1a(iii)]. The upper electrode is fixed under the upper cover, the lower electrode is fixed above the vibrator, and the four coils are fixed under the lower plate. The lower electrode, the lower plate, and the coil together form the vibrator, which is supported by four springs. The function of the spring is to limit the horizontal movement of the vibrator so that it can only move in the vertical direction. Figure S1 (Supporting Information) shows parts photos of the AMF-TENG. In Figure 1b, with the periodic change in the magnetic field, an induced electromotive force is generated in the coils, and the induced electromotive force generates a magnetic field. Currently, the magnetic fields of coils and magnets create attractive or repulsive Ampere forces and the coil drives the vibrator under the action of the ampere force vibration. At low speed, the force received by the coil is small, and the vibrator will not vibrate. As the speed increases, the vibrator will start to vibrate when the ampere force is greater than the electrostatic adsorption force. Figure 1c demonstrates the principle of the ampere force-driven generation unit. In step i, the position of the magnet is on the center line of two adjacent coils, and the lower-plate and the coil are located at the top, there is no current in coils. As the magnet array rotates and the magnet approaches the coils, the coils generates electric current due to electromagnetic induction in step ii, and coils generates a magnetic field opposite to the magnet to prevent magnetic flux of coil from changing. Therefore, coil drives lower-plate to move downward. In step iii, the coils are facing each other, and there

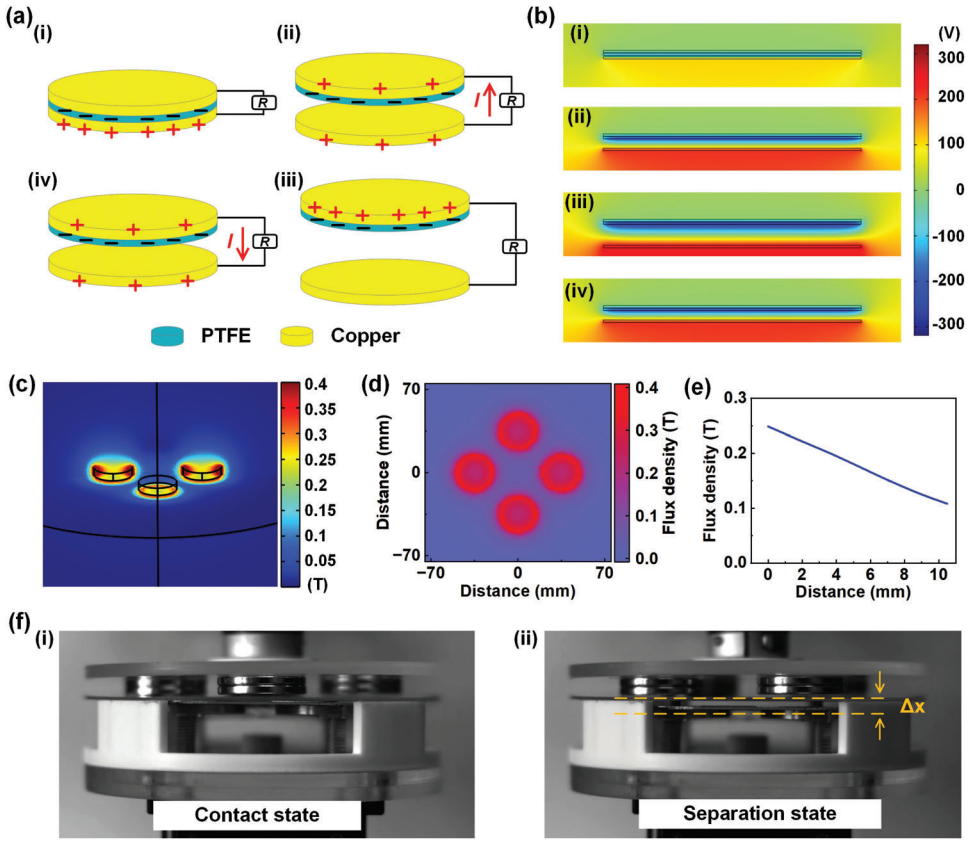

Figure 2. The alternating magnetic field-enhanced triboelectric nanogenerator (AMF-TENG) principle of operation and simulation. a) Four typical positions of the AMF-TENG. b) The space electric field of AMF-TENG simulated by COMSOL. c) The spatial magnetic field of the magnet matrix is simulated by COMSOL. d) Magnetic field distribution in the plane of the coil. e) A change in magnetic flux perpendicular to the magnet's center. f) Photographs of the change in position taken with a high-speed camera as the magnet approaches the coils during rotation.

is no current in the coil currently. When the magnet is farther and farther away from the coil, a current opposite to that in step ii is generated in coil in step iv. Preventing the coil's magnetic flux from changing, the current generates a magnetic field of the opposite polarity to the magnet, and the coil is subjected to an upward force to drive the lower plate upward movement. With periodic rotation, the lower plate and the upper plate are periodically contacted and separated. Note S1 (Supporting Information) analyzes and discusses the theory of alternating magnetic field driving generation unit.

AMF-TENG working principle can be seen in **Figure 2**a. In step i, the upper electrode and PTFE are held in contact by spring action. According to the triboelectric sequence, due to contact charging, electrons from the upper electrode are transferred to the PTFE resulting in a positive charge on the upper electrode, and an equal amount of negative charge on PTFE. The downward movement of the lower plate causes the triboelectric material distance to increase (step ii). As the separation distance increases, electrons move from the lower electrode to the upper electrode through the external circuit under the action of the electrostatic induction principle, causing the lower electrode to be positively charged to balance the electric field of PTFE (step iii). In step iv, electrons flow from the upper plate to the lower plate via external wires to generate a current in the opposite direction, while the lower plate moves up, and the periodic contact separation generates alternating current. To further study the electric field distribution of the AMF-TENG, simulation of Potential Distribution for Four Typical States Between Copper and PTFE Films Using COMSOL (COMSOL Multiphysics 6.0), is shown in Figure 2b. The distribution of the magnetic field has an impact on the ampere force. Using COMSOL to simulate the magnetic field of four rubidium magnets, the magnetic field distribution of the magnet array is obtained in Figure 2c. Based on the simulation results, the magnetic field strength distribution in the coil plane is calculated in Figure 2d. The magnetic field strength of the magnet is measured using a Gauss meter to be 243 mT, which agrees with the simulation of the magnetic field. Figure 2e shows a magnetic flux density distribution vertically from the magnet center. In simulations, increasing distance from a magnet reduces magnetic flux density. It is therefore important to fix the coil close to the magnet in order to maximize the ampere force produced by the coil. To verify the motion state of the generation unit driven by the alternating magnetic field. Use a high-speed camera to observe the motion state of AMF-TENG. When the servo motor is stationary, the upper electrode and the lower electrode of the generation unit are in contact with each other, and the relative displacement is 0 in Figure 2f(i). When the magnet array is driven by the servo motor, the upper and the lower electrodes are periodically contacted and separated with the movement of the magnet array [Figure 2f(ii), Video S1, Supporting Information].

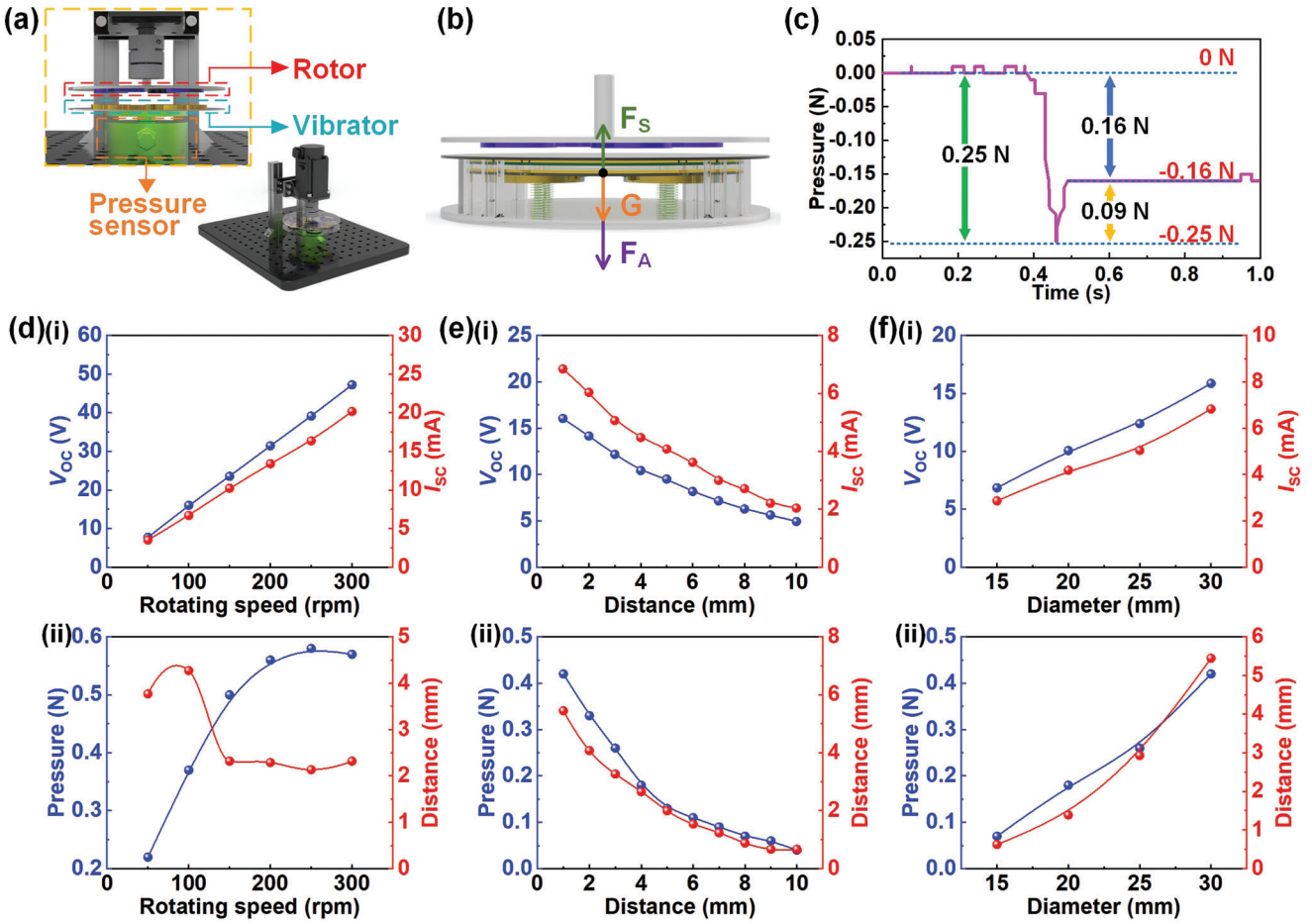

Figure 3. Alternating magnetic field-enhanced triboelectric nanogenerator (AMF-TENG) structural parameter optimization. a) Schematic diagram of pressure testing system. b) Force analysis of vibrator. c) Electrostatic adsorption force test in the AMF-TENG. d) Effect of rotation speed on voltage, current, pressure and amplitude of vibrator. e) An analysis of the effect of magnet to coil distance on AMF-TENG. f) The effect of the size change of the magnet on the vibrator.

2.2. Performances

A pressure test system is constructed using a servo motor and a pressure sensor to test the ampere force on the lower cover plate with the magnets fixed in **Figure 3**a. The pressure analysis of the vibrator is shown in Figure 3b. The vibrator receives gravity G at the same time, and elastic force F_S of spring and ampere force F_A act upon. Start G and F_S are the same in size, the force direction is opposite, and the resultant force received by the vibrator is F_A. In Figure 3c, the electrostatic adsorption force of generation unit is measured to confirm possibility of driving AMF-TENG with an alternating magnetic field. The upper cover and the vibrator are overlapped, the vibrator is fixed on the pressure sensor, and the upper cover is lifted suddenly. The pressure changes from 0 to −0.25 N, and then changes to −0.16 N, 0.16 N is the gravity of the upper cover, therefore, electrostatic adsorption force is 0.09 N. The size of the F_A is related to the voltage and current induced in the coil. The parameters of the structure and design are explored. In Figure 3d(i) and Figure S2a (Supporting Information), the output performance of coil is tested at different rotation speeds, and the open-circuit voltage (V_{OC}) and short-circuit current (I_{SC}) increased with the increasing rotation speed. With increases of rotational speed, pressure of vibrator increases, and the amplitude first increases and then decreases [Figure 3d(ii), Figure S3a, Supporting Information]. The increase in the amplitude at 50–100 rpm may have occurred. The effect of the distance between the magnet and the coils (100 rpm) is explored in Figure 3e. As the distance between the magnet and the coils increase, the V_{OC} and I_{SC} in the coils decreased with increasing distance [Figure 3e(i), Figure S2b, Supporting Information]. The pressure of the vibrator also decreases with the increasing distance. The amplitude of the vibrator appears to show a downward trend [Figure 3e(ii), Figure S3b, Supporting Information]. In Figure 3f, the effect of magnet size on the vibration form of the vibrator is explored (rotation speed is 100 rpm, distance is 1 mm). As the diameter of the magnet increases, the V_{OC} and I_{SC} rise with increasing magnet diameter [Figure 3f(i), Figure S2c, Supporting Information]. The ampere force and amplitude of vibrator increase with diameter with magnet. [Figure 3f(ii), Figure S3c, Supporting Information].

Because the generation unit can perform contact separation motion driven by the ampere force, to test the performance of

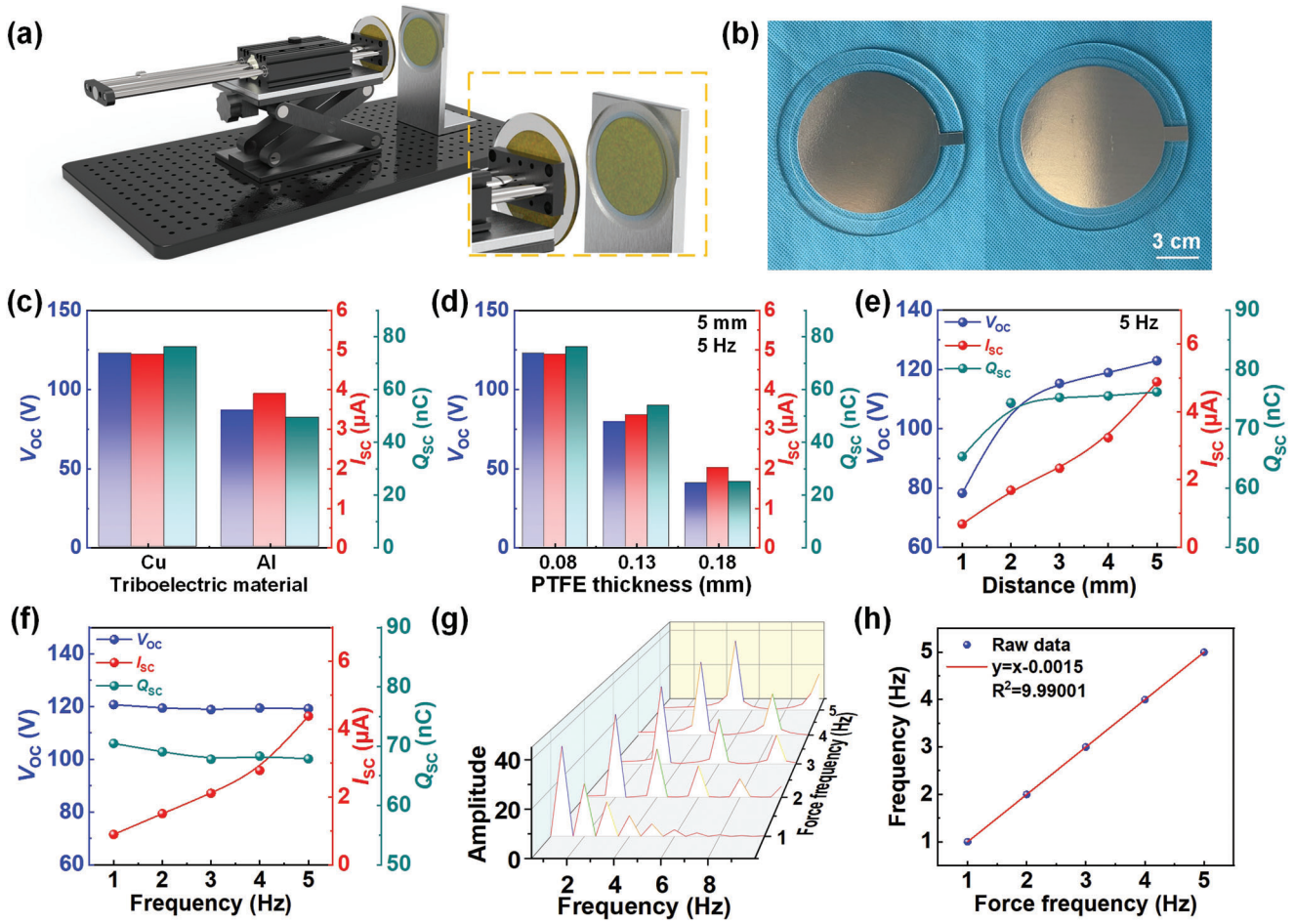

Figure 4. Test of generation unit output performance. a) Generation unit test platform constructed by LinMot. b) Photograph of the two electrodes in the generation unit. c) Effect of electrode material. d) Effect of PTFE film thickness on output performance. e) Output test of the generation unit with separation distance. f) Influence of contact frequency on generation unit performance. g) FFT of generation unit voltage signal at different frequencies. h) Frequency fitting analysis.

generation unit, the generation unit for standardized tests is driven by a linear motor. **Figure 4**a shows the test system driven by the linear motor. One electrode of the generation unit fixed on one end of the linear motor, and the other electrode is fixed on the optical table. Figure 4b shows the two electrodes of generation unit. The diameter of the copper electrodes is 90 mm, and a copper is covered with PTFE. The output performance of generation unit has a great relationship with the triboelectric materials and material thickness. In Figure 4c and Figure S4 (Supporting Information), 0.08 mm thick PTFE is used as the negative triboelectric material. When Cu is used as a positive triboelectric material, V_{OC}, I_{SC}, and transfer charge (Q_{SC}) are 122.7 V, 4.9 μA, and 76.1 nC, respectively; when Al is used as positive triboelectric material, V_{OC}, I_{SC}, and Q_{SC} are 86.6 V, 3.9 μA, and 49.3 nC, respectively. Therefore, using Cu as a positive triboelectric material has better performance. As shown in Figure 4d and Figure S5 (Supporting Information), change the thickness of the PTFE film. When the PTFE film increased from 0.08 to 0.18 mm, the V_{OC}, I_{SC}, and Q_{SC} of generation unit showed downward trend, so 0.08 mm is chosen. The relative displacements of the two electrodes of the generation unit are different under the driving of the amperometric force, so the changes in the displacement distance and the output performance of the generation unit are explored in Figure 4e and Figure S6 (Supporting Information). Experiments show that under a fixed frequency drive of 5 Hz, with the increasing displacement, the output properties of generation unit all show an upward trend, which may be due to the small displacement distance and the degree of contact between the two electrodes of the generation unit with different displacements. At a relative displacement of 5 mm, different frequencies are used to drive the generation unit. In Figure 4f and Figure S7 (Supporting Information), when the displacement is fixed, the V_{OC} and Q_{SC} of generation unit remain unchanged with increasing frequency, and the I_{SC} increases with increasing frequency. The output frequency of the generation unit is related to the frequency of the driving force, which is expected to use the generation unit to detect the frequency of the driving force. In Figure 4g, the fast Fourier transform of voltage waveform obtains the spectral information at different frequencies. Fitting the frequency of the generation unit with the driving frequency in Figure 4h shows that the

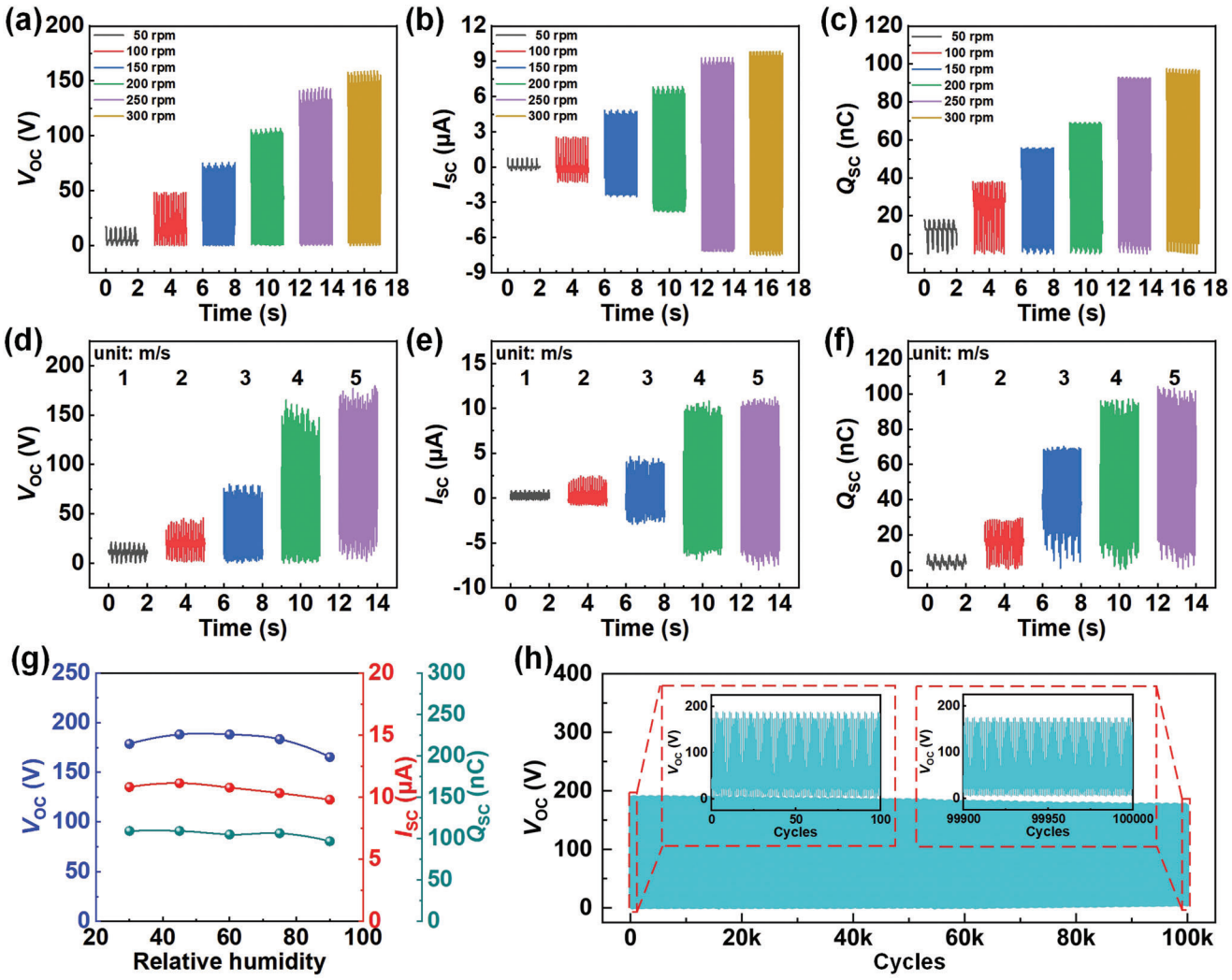

Figure 5. Alternating magnetic field-enhanced triboelectric nanogenerator (AMF-TENG) tested in simulated wind environment. a) V_{OC}, b) I_{SC}, and c) Q_{SC} at different rotation speeds. d) V_{OC}, e) I_{SC}, and f) Q_{SC} of AMF-TENG at different wind speeds. g) Effect of relative humidity on AMF-TENG voltage. h) Stability test of the AMF-TENG.

generation unit can accurately monitor the external frequency information, which makes the AMF-TENG promising as a self-powered frequency sensor.

The AMF-TENG is driven by a servo motor. In **Figure 5**a, when the speed increases from 50 to 300 rpm, V_{OC} increases from 16.5 to 158.6 V, I_{SC} increases from 0.71 to 9.8 μA (Figure 5b), and the Q_{SC} increases from 17.9 to 97.6 nC (Figure 5c). Then, taking wind energy as an example, using AMF-TENG in a breeze environment is tested. In the wind speed of 1–5 m s^{-1}, V_{OC} increases from 20.9 to 179.3 V (Figure 5d), I_{SC} increases from 0.9 to 11.3 μA (Figure 5e), and the Q_{SC} increases from 8.8 to 104.1 nC (Figure 5f). The contact force between the two electrodes here changes with the change of the rotational speed [Figure 3d(ii)]. When the pressure increases, the contact area between the two electrodes increases, so the V_{OC} and short I_{SC} also tend to increase. TENGs often face harsh working conditions in outdoor environments. The effect of relative humidity is verified at a speed of 300 rpm. The relative humidity increased from 30% to 90%. V_{OC}, I_{SC}, and Q_{SC} are maintained at 92.6%, 92.5%, and 88.6% respectively. (Figure 5g, Figure S8, Supporting Information). Therefore, the AMF-TENG can adapt to the harsh working environment outdoors, which may be attributed to the good sealing of the AMF-TENG. At 300 rpm, after 100 K cycles, the V_{OC} is reduced from 188.2 to 173.7 V, and the performance remained at 92.5%. The AMF-TENG shows good stability.

2.3. Demonstration

Figure 6a illustrates the working state diagram of AMF-TENG. In conditions of 5 m s^{-1}, AMF-TENG get a maximum output of 0.68 mW when connected to load at 10 MΩ (Figure 6b). The cut-in wind speed of this work has a great advantage compared with the previous works in Figure 6c. The AMF-TENG charges capacitors with diverse capacities in Figure 6d, with good charging ability. AMF-TENG works at a wind speed of 1 m s^{-1}, and it

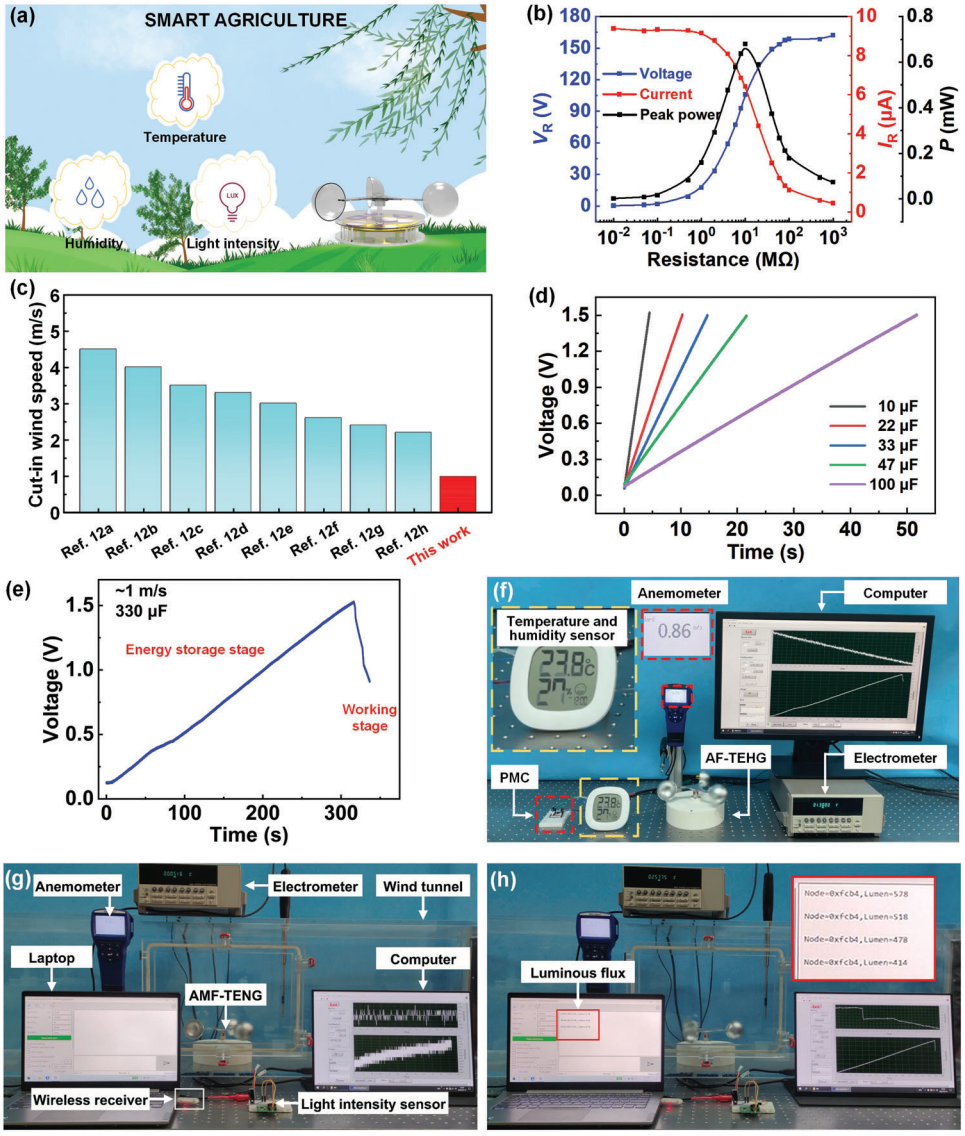

Figure 6. Application of alternating magnetic field-enhanced triboelectric nanogenerator (AMF-TENG) for self-powered sensing in smart agriculture. a) Application concept of AMF-TENG in an agricultural breeze environment. b) AMF-TENG externally connected with different loads. c) Cut-in speed of this work compared with previous work.[12] d) AMF-TENG charging commercial capacitors with different capacities at 1 m s^{-1}. e) The AMF-TENG charges a commercial capacitor of 330 μF to 1.5 V within 316 s at 1 m s^{-1}. f) AMF-TENG lights up a temperature and humidity sensor at 1 m s^{-1}. g) Wireless light intensity sensing system based on AMF-TENG. h) Demonstration of wireless light intensity sensing.

takes 316 s to charge a capacitor of 330 μF to 1.5 V (Figure 6e), and supply power to the temperature and humidity sensor and work smoothly. The circuit diagram for charging the capacitor is shown in Figure S9 (Supporting Information). Video S2 (Supporting Information) details the demonstration process of lighting up the temperature and humidity sensors. An outdoor demonstration video (Video S3, Supporting Information) is supplemented to illustrate the harvesting ability of AMF-TENG in a real natural wind environment. In Figure S10 (Supporting Information), the AMF-TENG is placed in an outdoor environment. Driven by natural wind, AMF-TENG charges a 220 μF capacitor, and the voltage of the capacitor rises to 1.7 V after about 7 min. AMF-TENG successfully powered a commercial temperature and humidity sensor. Figure 6f shows the demonstration of AMF-TENG powering a temperature and humidity sensor at 1 m s^{-1} smart agriculture. Wireless transmission function is necessary for IoT nodes. Figure 6g shows the wireless light intensity demonstration system built based on AMF-TENG. In this system, AMF-TENG is used to harvest wind energy, the wireless light intensity sensor is used to test the ambient light intensity and send information, and the laptop and wireless receiver are used to receive the signal from the sensor. As shown in Figure 6h, AMF-TENG charged a 3300 μF commercial capacitor to 3.7 V for 125 min under a wind speed of 5 m s^{-1}, and then the light intensity sensor started to work, and the laptop successfully received and displayed the light intensity information of the current environment (Figure S11, Video S4, Supporting Information). This system demonstrates the possibility of AMF-TENG to power IoT nodes.

3. Conclusions

In conclusion, an ampere force-based AMF-TENG is proposed for efficient low-speed flow energy harvesting and self-powered sensing. AMF-TENG is a high-efficiency low-speed wind energy harvesting strategy based on coupled coil and magnet electromagnetic induction, triboelectric, and electrostatic induction effects of mechanical-electric energy conversion, enabling TENG to harvest wind energy down to 1 m s^{-1}. Under the movement of the external magnetic field, coils generate induced current, ampere force is generated due to the magnetic effect of the current and the action of the external magnetic field, and the ampere force drives the vertical contact-separation TENG. Since the current in the coil decreases with decreasing the rotation speed, the resistance received by the AMF-TENG during low-speed rotation will also decrease, so the collection of low-speed wind energy (1 m s^{-1}) can be realized, which greatly broadens the range of wind speed in TENG. V_{OC} of AMF-TENG is 20.9 to 179.3 V at wind speeds of 1 to 5 m s^{-1}. After 100 K cycles of continuous operation, the AMF-TENG voltage is maintained at about 92.5%. A capacitor of 330 μF can be charged to 1.5 V at 1 m s^{-1}. Based on AMF-TENG, self-powered sensing applications in smart agriculture are designed, which reaches low-speed wind harvesting in natural environment and supplies power for agricultural temperature and humidity sensors and wireless light intensity sensor. This study provides a new strategy for low-altitude, low-speed wind energy harvesting.

4. Experimental Section

Fabrication of the AMF-TENG: The stator and upper cover were cut from a 1 mm acrylic sheet. The mover was cut from a 3 mm acrylic sheet. Magnets were used to create an alternating magnetic field, and the magnets were fixed on the rotor with double-sided tape. The coils were fixed on the vibrator, and the number of turns of the coil was 2000. The shell was printed with a 3D printer, and the printing material was poly lactic acid. The model of the PTFE film was ASF-110FR, and the manufacturer was Chukoh Chemical Industries, Ltd. of Japan. The manufacturer of the copper foil was Xinshi of China. The schematic flow diagram for fabricating AMF-TENG is presented in detail in Figure S12 (Supporting Information).

Electrical Measurement: An AC servo motor (HG-KR43J, Mitsubishi Electric, Japan) provided the rotational excitation. A linear motor (PR-52, LinMot, Switzerland) provided external linear excitation. A programmable electrometer (6514, Keithley, USA) was used for output performance testing. The stress test was tested and collected using a force sensor (AR-DN31, ARIZON, China) and a signal collector (USB06, ARIZON, China). A laser displacement sensor (ILD1402, Micro-Epsilon, Germany) was used to test the vibration displacement of the vibrator, and a programmable humidity chamber (Y-HF-960L, China) was used to simulate relative humidity changes.

Pressure Measurement of Vibrator: The vibrator was fixed on the pressure sensor with double-sided tape, and then the rotor was connected to the servo motor with a coupling. When the servo motor drove the rotor to rotate, the computer software supporting the pressure sensor was used to record the pressure curve. The vertical distance between the rotor and the vibrator could be adjusted by controlling the height of the servo motor. It is worth paying special attention that all parts of the pressure test system should not use magnetic materials, otherwise it would affect the test results.

Amplitude Measurement of Vibrator: A laser displacement sensor was used to measure the amplitude of the vibrator, and a light and small reflective plate was fixed on the vibrator to reflect the laser light of the laser displacement sensor. When the servo motor drove the rotor to rotate to vibrate the vibrator, the reflective plate on the vibrator could make the vibration amplitude of the vibrator be received by the laser displacement sensor. The signal of the laser displacement sensor was collected through the data acquisition card, and the supporting software of the data acquisition card is based on LabVIEW.

Supporting Information

Supporting Information is available from the Wiley Online Library or from the author.

Acknowledgements

The authors are grateful for the support from the Beijing Natural Science Foundation (No. 3222023), and the National Key Research & Development Project from the Minister of Science and Technology (Nos. 2021YFA1201601 and 2021YFA1201604).

Conflict of Interest

The authors declare no conflict of interest.

Data Availability Statement

The data that support the findings of this study are available from the corresponding author upon reasonable request.

Keywords

alternating magnetic field, low-speed flow energy, self-powered, smart agriculture, triboelectric nanogenerators

Received: May 2, 2023
Revised: May 24, 2023
Published online:

[1] H. Fell, A. Gilbert, J. D. Jenkins, M. Mildenberger, *Nat. Energy* **2022**, *7*, 25.
[2] a) W. C. He, C. C. Shan, S. K. Fu, H. Y. Wu, J. Wang, Q. J. Mu, G. Li, C. G. Hu, *Adv. Mater.* **2023**, *35*, 2209657; b) Z. W. Ren, X. Liang, D. Liu, X. J. Li, J. F. Ping, Z. M. Wang, Z. L. Wang, *Adv. Energy Mater.* **2021**, *11*, 2101116.
[3] a) L. Zhang, B. B. Zhang, J. Chen, L. Jin, W. L. Deng, J. F. Tang, H. T. Zhang, H. Pan, M. H. Zhu, W. Q. Yang, Z. L. Wang, *Adv. Mater.* **2016**, *28*, 1650; b) J. Mu, J. Zou, J. Song, J. He, X. Hou, J. Yu, X. Han, C. Feng, H. He, X. Chou, *Energy Convers. Manage.* **2022**, *254*, 115151.
[4] a) Q. Tian, G. Huang, K. M. Hu, D. Niyogi, *Energy* **2019**, *167*, 1224; b) S. Yong, J. Y. Wang, L. J. Yang, H. Q. Wang, H. Luo, R. J. Liao, Z. L. Wang, *Adv. Energy Mater.* **2021**, *11*, 2101194.
[5] a) C. Zhang, Y. Liu, B. Zhang, O. Yang, W. Yuan, L. He, X. Wei, J. Wang, Z. L. Wang, *ACS Energy Lett.* **2021**, *6*, 1490; b) B. Chen, Y. Yang, Z. L. Wang, *Adv. Energy Mater.* **2018**, *8*, 1702649.
[6] a) F.-R. Fan, Z.-Q. Tian, Z. L. Wang, *Nano Energy* **2012**, *1*, 328; b) Z. L. Wang, *Nano Energy* **2020**, *68*, 104272; c) L. Q. Liu, X. Y. Yang, L. L. Zhao, H. X. Hong, H. Cui, J. L. Duan, Q. M. Yang, Q. W. Tang, *ACS Nano* **2021**, *15*, 9412; d) Z. L. Wang, A. C. Wang, *Mater. Today* **2019**, *30*, 34.

[7] a) C. Ye, K. Dong, J. An, J. Yi, X. Peng, C. Ning, Z. L. Wang, *ACS Energy Lett.* **2021**, *6*, 1443; b) H. Hong, X. Y. Yang, H. Cui, D. Zheng, H. Y. Wen, R. Y. Huang, L. Q. Liu, J. L. Duan, Q. W. Tang, *Energy Environ. Sci.* **2022**, *15*, 621; c) L. J. Xie, N. N. Zhai, Y. N. Liu, Z. Wen, X. H. Sun, *Research* **2021**, *2021*, 9143762.

[8] a) B. S. Zhang, S. Zhang, W. B. Li, Q. Gao, D. Zhao, Z. L. Wang, T. H. Cheng, *ACS Nano* **2021**, *15*, 20278; b) Y. J. Tang, H. Zhou, X. P. Sun, N. H. Diao, J. B. Wang, B. S. Zhang, C. Qin, E. J. Liang, Y. C. Mao, *Adv. Funct. Mater.* **2020**, *30*, 1907893; c) K. Q. Fan, D. M. Wei, Y. Zhang, P. H. Wang, K. Tao, R. S. Yang, *Nano Energy* **2021**, *90*, 106576.

[9] S. Yong, H. Wang, Z. Lin, X. Li, B. Zhu, L. Yang, W. Ding, R. Liao, J. Wang, Z. L. Wang, *Adv. Energy Mater.* **2022**, *12*, 2202469.

[10] a) B. S. Zhang, Y. J. Tang, R. R. Dai, H. Y. Wang, X. P. Sun, C. Qin, Z. F. Pan, E. J. Liang, Y. C. Mao, *Nano Energy* **2019**, *64*, 103953; b) M. Wang, J. H. Zhang, Y. J. Tang, J. Li, B. S. Zhang, E. J. Liang, Y. C. Mao, X. D. Wang, *ACS Nano* **2018**, *12*, 6156.

[11] a) Z. L. Wang, *Rep. Prog. Phys.* **2021**, *84*, 096502; b) S. H. Xu, X. P. Fu, G. X. Liu, T. Tong, T. Z. Bu, Z. L. Wang, C. Zhang, *iScience* **2021**, *24*, 102318.

[12] a) E. Su, H. Li, J. Zhang, Z. Xu, B. Chen, L. N. Y. Cao, Z. L. Wang, *Adv. Funct. Mater.* **2023**, *33*, 2214934; b) X. M. Fan, J. He, J. L. Mu, J. C. Qian, N. Zhang, C. J. Yang, X. J. Hou, W. P. Geng, X. D. Wang, X. J. Chou, *Nano Energy* **2020**, *68*, 104319; c) Y. Fang, T. Y. Tang, Y. F. Li, C. Hou, F. Wen, Z. Yang, T. Chen, L. N. Sun, H. C. Liu, C. K. Lee, *iScience* **2021**, *24*, 102300; d) X. Li, Y. Cao, X. Yu, Y. Xu, Y. Yang, S. Liu, T. Cheng, Z. L. Wang, *Appl. Energy* **2022**, *306*, 117977; e) Y. Luo, P. Chen, L. N. Y. Cao, Z. Xu, Y. Wu, G. He, T. Jiang, Z. L. Wang, *Adv. Funct. Mater.* **2022**, *32*, 2205710; f) Y. Gui, Y. Wang, S. He, J. Yang, *Energy Convers. Manage.* **2022**, *269*, 116098; g) K. Fan, C. Chen, B. Zhang, X. Li, Z. Wang, T. Cheng, Z. L. Wang, *Appl. Energy* **2022**, *328*, 120218; h) H. X. Zou, L. C. Zhao, Q. Wang, Q. H. Gao, G. Yan, K. X. Wei, W. M. Zhang, *Nano Energy* **2022**, *95*, 106990.